IIETA International Information and Engineering Technology Association
Advancing the World of Information and Engineering

Mathematical Modelling of Engineering Problems
Vol. 13, No. 8, August, 2026, pp. 1009-1015
Journal homepage: http://iieta.org/journals/mmep

A Mathematical Framework for Radar Stability Budgets Illustrated by Normalized Signal Models

Vladimir Konchin[1*], Irina Vornacheva[2], Dmitrii Zhilyakov[3]

[1] Department of Electrical Engineering and Electric Power Engineering, Kursk State Agrarian University named after I. I. Ivanov, Kursk 305021, Russia
[2] Department of Electric Power Engineering and Electrical Engineering, Southwest State University, Kursk 305040, Russia
[3] Department of Accounting and Finance, Kursk State Agrarian University named after I. I. Ivanov, Kursk 305021, Russia

Corresponding Author Email: konchin98@mail.ru

Copyright: ©2026 The authors. This article is published by IIETA and is licensed under the CC BY 4.0 license (http://creativecommons.org/licenses/by/4.0/).

https://doi.org/10.18280/mmep.130803

Received: 3 August 2026
Revised: 28 September 2026
Accepted: 7 October 2026
Available online: 31 October 2026

Keywords:
active phased array, hardware stability, moving-target indication, pulse compression, radar detection, uncertainty propagation

ABSTRACT

Hardware stability requirements depend on the radar-processing metric they must protect. This study formulates a performance-to-error framework and illustrates it with normalized signal models, without measured component data. The cases comprised a linear-frequency-modulated (LFM) pulse with a time-bandwidth product of 64, Barker-13 compression, a two-pulse moving-target-indication canceller, and an ideal 32-element broadside array. For independent square-law pulse decisions, a 3-out-of-4 rule with a packet false-alarm probability of 10^{-6} and a detection-probability decrease from 0.90 to 0.85 allowed a 0.332 dB signal-to-noise-ratio (SNR) loss. The corresponding deterministic chirp-rate-error boundary was 1.83%. Under independent zero-mean Gaussian phase errors, the other boundaries were 10.59° per-chip root-mean-square (RMS) phase error for mean Barker-13 peak sidelobe ratio (PSLR) degradation, 1.81° aggregate differential inter-pulse RMS phase error for mean clutter residual, and 19.77° element RMS phase error for mean array gain. These quantities have different definitions and are not interchangeable component specifications. Equal-share source values and a specified correlated-source example illustrate covariance arithmetic. The results identify the governing metric in each model; practical hardware allocation still requires source sensitivities, measured covariance, and joint nonlinear verification.

1. INTRODUCTION

Pulse compression, coherent integration, moving-target indication (MTI), and digital beamforming depend on waveform and channel coherence. Classical radar detection theory relates detection probability to statistical assumptions about the signal and noise [1]. In hardware, errors arise in frequency synthesis, modulation, amplification, conversion, sampling, and array calibration. A component specification must therefore relate to the processing metric it is intended to protect.

Prior work already links particular hardware errors to radar performance. Siddiq et al. [2] derived source phase-noise limits for frequency-modulated continuous-wave (FMCW) radar and examined decorrelation in coherent mixing. Tschapek et al. [3] separated systematic phase distortion from stochastic phase noise and retained its spectral structure. These studies establish that phase-noise sensitivity depends on the signal model and processing operation; a single integrated phase-error value cannot replace that information. For pulse compression, Bharadwaj and Chandrasekar [4] examined phase-noise effects on sidelobes. Torres et al. [5] explicitly connected waveform design to high-level weather-radar requirements, while enhanced matched filtering [6] addressed sidelobe suppression. Thus, requirement-driven design and phase-error sensitivity are established subjects.

Related studies provide more specific links between hardware instability and the processed signal. Thurn et al. [7] related the source phase-noise profile and range correlation to FMCW ranging uncertainty. Siddiq et al. [8] modeled the contribution of sampling-clock jitter to the phase noise of sampled homodyne signals. Levy et al. [9] examined coherent integration loss under nonstationary phase noise, while Birkenhauer et al. [10] described over-the-air measurement of radar phase-noise spectra. These results show why source spectra, timing, and the receiver architecture must be specified before aggregate signal-error limits can be assigned to hardware.

Spatial processing imposes additional constraints. Geiß et al. [11] related array calibration errors to image distortions and bounded their effects. Beacon-based calibration [12] provides measured channel corrections, whereas auxiliary-array selection [13] concerns adaptive sidelobe cancellation. Studies [12, 13] establish relevant calibration and cancellation contexts; they do not validate a scalar mean-gain budget or the allocation proposed here. Schmid et al. [14] derived worst-case and statistical beam-pattern deviation bounds for calibration errors and mutual coupling, providing a

complementary basis for array tolerance analysis. The present array example evaluates only mean gain under independent element phase errors.

This study organizes these function-specific relations into a common sequence: define a performance limit, select an observable metric, identify an error coordinate, and distribute its variance when a stochastic source model is available. The contribution is a mathematical framework illustrated by normalized cases, rather than a complete radar allocation validated with component records. The aim is to compare governing constraints for linear-frequency-modulated (LFM) chirp-rate mismatch, Barker-13 chip phase error, two-pulse MTI differential phase error, and mean array gain. The numerical examples establish aggregate boundaries and illustrate equal-share covariance arithmetic; they do not identify source-specific hardware sensitivities.

2. METHODOLOGY

2.1 Performance limits and observable signal metrics

Figure 1 shows the proposed hierarchy. A radar-level limit is converted into a metric at the output of a matched filter, canceller, or beamformer. An error model then relates that metric to waveform or channel perturbations. Hardware allocation additionally requires source sensitivities and covariance. The present examples illustrate the first mappings and a normalized equal-share calculation.

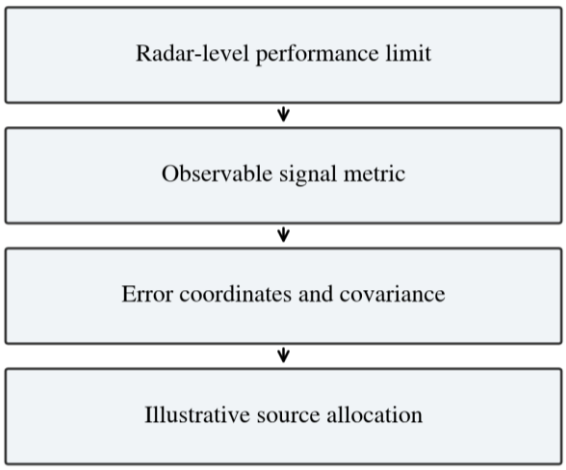


Figure 1. Performance-to-error hierarchy and illustrative allocation

For the j-th radar characteristic, the general mapping is written as

$$\Delta C_j = F_j(q), \mathbf{q} = G(\mathbf{x}) \tag{1}$$

where, ΔC_j is the admissible deterioration of a radar-level characteristic, $\mathbf{q}$ is the vector of observable signal metrics, and $\mathbf{x}$ contains deterministic biases and random hardware errors. The first mapping depends on the detection, resolution, cancellation, or beamforming algorithm. The second mapping can be obtained analytically, by circuit-level simulation, or by a controlled numerical perturbation of the signal-processing chain.

For pulse-compression radar, the mismatched-filter output is

$$y(\tau;\mathbf{x}) = \int s(t;\mathbf{x}) s_0^*(t-\tau)\,\mathrm{d}t \tag{2}$$

where, $s_0(t)$ is the nominal waveform and $s(t;\mathbf{x})$ is the waveform containing hardware-induced errors. Three complementary metrics are used: the normalized main-peak amplitude $a = |y(0;\mathbf{x})|/|y(0;\mathbf{0})|$, the peak sidelobe ratio (PSLR) $\delta = \max_{\tau\notin\mathcal{M}}|y(\tau;\mathbf{x})|/|y(0;\mathbf{x})|$, and the relative half-power width increase $\Delta_\tau = [\tau_{3\mathrm{dB}}(\mathbf{x}) - \tau_{3\mathrm{dB}}(\mathbf{0})]/\tau_{3\mathrm{dB}}(\mathbf{0})$. Here, $\mathcal{M}$ denotes the nominal mainlobe interval. For random errors, the mean and variance of each metric are retained rather than only its nominal value.

2.2 Detection-probability mapping

When an m-pulse observation uses a "k out of m" decision rule, the packet-level probability is related to the single-pulse probability p by

$$P(p;k,m) = \sum_{r=k}^{m} \frac{m!}{r!\,(m-r)!} p^r (1-p)^{m-r} \tag{3}$$

Eq. (3) assumes independent pulse decisions with the same single-pulse probability. It was applied separately to detection and false alarms. The detection model used a nonfluctuating target, additive circular complex Gaussian noise, a square-law detector, and a fixed threshold. The normalized detector statistic had two degrees of freedom: a central chi-square distribution under noise alone and a noncentral chi-square distribution with noncentrality $2v$ under signal plus noise. Here v is the single-pulse signal-to-noise-ratio (SNR). The relation is $p_D = Q_1(\sqrt{(2v)}, \sqrt{\eta})$, where Q_1 is the first-order Marcum Q function and $\eta = -2 \ln p_F$. A fixed receive filter and unchanged noise power were assumed. An amplitude mismatch factor a therefore changed SNR to $v' = a^2 v$.

The calculation used a 3-out-of-4 rule, packet false-alarm probability $P_F = 10^{-6}$, baseline packet detection probability $P_{D,0} = 0.90$, and minimum packet detection probability $P_{D,\min} = 0.85$. These are prescribed numerical conditions, not operational requirements for a particular radar. Correlated pulse decisions, target fluctuations, adaptive thresholds, and clutter would require a different probability mapping.

2.3 Criteria for moving-target indication and active arrays

For a two-pulse canceller, let φ_n be the zero-mean residual phase of pulse n and $\Delta\varphi_n = \varphi_n - \varphi_{n-1}$ the differential inter-pulse phase error. A stationary unit-amplitude return produces residual power $|1 - \exp(j\Delta\varphi_n)|^2$. If $\Delta\varphi_n$ is Gaussian with variance $\sigma_{\Delta\varphi}^2$, its mean residual power is

$$r_{\mathrm{MTI}} = 2\left[1 - \exp\left(-\frac{\sigma_{\Delta\phi}^2}{2}\right)\right] \approx \sigma_{\Delta\phi}^2 \tag{4}$$

The phase-difference variance is $\sigma_{\Delta\varphi}^2 = \mathrm{Var}(\varphi_n) + \mathrm{Var}(\varphi_{n-1}) - 2\,\mathrm{Cov}(\varphi_n, \varphi_{n-1})$. For a stationary process with pulse variance σ_p^2 and lag-one correlation ρ_1, it becomes $2\sigma_p^2(1 - \rho_1)$. Independent consecutive pulse errors therefore give $\sigma_p = \sigma_{\Delta\varphi}/\sqrt{2}$; this conversion is invalid without the temporal covariance. The residual in Eq. (4) is normalized to the power of one uncancelled pulse. Its −30 dB limit is not an MTI improvement factor normalized to target gain.

For a stationary phase process with one-sided phase-noise power spectral density $S_\varphi(f)$, $\sigma_{\Delta\varphi}^2 = 4\int_0^\infty S_\varphi(f)\,\sin^2(\pi f T_r)\,df$,

where T_r is the pulse-repetition interval. The integral must use the phase process at the canceller input, including relevant transfer functions and measurement bandwidth. Thus, an oscillator or clock specification requires T_r and a spectral or temporal model; it cannot be inferred from $\sigma_{\Delta\varphi}$ alone.

For an N-element broadside array with equal amplitudes and independent zero-mean Gaussian element phase errors of standard deviation σ_a, the mean normalized coherent power gain is

$$g = \frac{1}{N} + \left(1 - \frac{1}{N}\right) exp(-\sigma_a^2) \tag{5}$$

where $g = E\{|N^{-1}\sum \exp(j\varphi\ell)|^2\}$, $\varphi\ell$ is the phase error of element ℓ. Eq. (5) concerns this mean alone. Beam-pointing displacement, sidelobe level, and the probability of an individual gain loss were not evaluated. Table 1 distinguishes the quantities actually calculated from error classes that would require additional models.

Table 1. Evaluated quantities and scope of the numerical cases

Case	Evaluated Coordinate and Metric
Linear-frequency-modulated (LFM)	Prescribed chirp-rate mismatch; detection-derived peak loss and half-power width
Barker-13	Independent per-chip Gaussian phase error; mean peak loss and mean peak sidelobe ratio (PSLR)
Two-pulse moving-target indication (MTI)	Gaussian differential phase error; mean residual power
32-element array	Independent element Gaussian phase error; mean coherent power gain

2.4 Covariance propagation and allocation

Let z_i be a selected signal metric and let x_r represent the error generated by the r-th hardware source. Linearization about the nominal operating point gives

$$\Delta z_i \approx \sum_{r=1}^{R} S_{ir}\, x_r, \qquad S_{ir} = \left.\frac{\partial z_i}{\partial x_r}\right|_{\mathbf{x=0}} \tag{6}$$

With the sensitivity row vector $\mathbf{S}_i$ and the hardware-error covariance matrix $\mathbf{\Sigma}_x$, the metric variance is

$$\sigma_{z_i}^2 = \mathbf{S}_i \mathbf{\Sigma}_x \mathbf{S}_i^{\mathrm{T}} \tag{7}$$

For independent sources, Eq. (7) reduces to $\sigma_{z_i}^2 = \sum_r S_{ir}^2\, \sigma_{x_r}^2$. If a fraction β_{ir} of the allowable variance is assigned to source r, with $\beta_{ir} \geq 0$ and $\sum_r \beta_{ir} = 1$, its allowable standard deviation is

$$\sigma_{x_r,\max}^{(i)} = \frac{\sqrt{\beta_{ir}}\, \sigma_{z_i,\max}}{|S_{ir}|} \tag{8}$$

For each source, the overall allowable standard deviation is the minimum of its criterion-specific values in Eq. (8). This construction assumes independent sources and a nonzero sensitivity for the criterion concerned. A zero sensitivity imposes no first-order restriction and requires higher-order examination. Deterministic biases contribute through the signed sum of sensitivity times bias; root-sum-square (RSS) addition is not a worst-case bias rule. Correlated-source allocation requires the complete covariance expression in Eq. (7), not Eq. (8) alone.

Variance is the square of the standard deviation. For zero-mean errors, root-mean-square (RMS) equals standard deviation; a biased error has RMS² = variance + bias². Moreover, peak loss and mean coherent-gain loss are locally even functions of phase or chirp mismatch and can have zero gradient at the nominal point. Eqs. (6)–(8) must not be applied to those losses using a zero first derivative. The illustrative allocations below operate in additive error coordinates; the processing loss is then evaluated with its nonlinear model.

A practical implementation would define each protected limit, measure or simulate source perturbations, estimate sensitivities, construct the source covariance matrix, and solve the applicable allocation constraints. It would then check the full nonlinear chain at the combined errors. This study did not perform those operations with measured hardware records. The equal-share examples in Section 3.4 demonstrate only the specified normalized source model.

2.5 Numerical models and design limits

The calculations used normalized complex baseband signals. The LFM pulse was $s_0(t) = \exp(j\pi Kt^2)$, $-T/2 \leq t \leq T/2$, with $KT^2 = BT = 64$. Here T is the pulse duration, and B is the bandwidth. A uniform grid of $N_s = 1{,}024$ points included both endpoints. The perturbed pulse used $K(1 + \varepsilon_K)$, where the prescribed chirp-rate mismatch ε_K ranged from 0 to 6% in 0.25-percentage-point increments. Discrete linear correlation implemented Eq. (2). The nominal-delay peak was normalized by N_s; half-power crossings were linearly interpolated. Only the chirp rate was perturbed. Start frequency, duration, general sweep nonlinearity, and phase noise were not evaluated in this case.

The Barker-13 sequence [1, 1, 1, 1, 1, −1, −1, 1, 1, −1, 1, −1, 1] used 12 samples per chip. Each trial assigned independent zero-mean Gaussian errors to the 13 chips, with one constant phase error throughout each chip. Their common standard deviation σ_b was swept from 0 to 30° in 1° increments, with 1,200 trials per level. NumPy default_rng(2026), using PCG64, generated a 1,200 × 13 standard-normal matrix. The same matrix was scaled at each level. The nominal-delay peak was used for normalization. PSLR was 20 $\log_{10}$ of the largest sidelobe-to-peak amplitude ratio, with |lag| < 12 samples excluded. Degradation was measured relative to $-20 \log_{10}(13) = -22.28$ dB.

The MTI case evaluated Eq. (4) from 0.1 to 5.0° in 0.1° increments. The array comprised 32 ideal half-wavelength-spaced, equal-amplitude elements steered to broadside. A separate default_rng(2026) call generated a 6,000 × 32 standard-normal matrix, reused across the 0–30° sweep. The mean power gain was averaged before conversion to decibels and compared with Eq. (5). Angular quantities were converted to radians. The prescribed limits were 0.5 dB for peak or mean-gain loss, 3 dB for mean Barker-13 PSLR degradation, and −30 dB for mean stationary-clutter residual. Section 2.2 supplied the additional detection-derived LFM loss limit.

2.6 Verification and reproducibility protocol

The numerical boundaries were located on the relevant monotonic branch. Adjacent sweep levels bracketing each

limit were identified, and the crossing was linearly interpolated in the error coordinate. Values outside the simulated range were not extrapolated. Analytical MTI and array roots were also calculated directly. Boundary values are model-dependent numerical estimates; the final digits do not represent experimental accuracy.

The LFM correlation was recalculated from the sampled waveforms. The MTI residual was checked against Eq. (4), and the array Monte Carlo mean was compared with Eq. (5). For Barker-13, the sample mean and standard error $s_d/\sqrt{1200}$ were calculated at each level, with s_d the sample standard deviation. Pointwise approximate 95% confidence intervals for the mean used mean $\pm t_{0.975,1199}\ s_d/\sqrt{1200}$. They quantify Monte Carlo uncertainty of the mean, not the distribution of individual sidelobe responses or a simultaneous confidence band for the whole sweep. The shared draws correlate the sweep estimates without changing their marginal distributions.

The detection mapping was calculated before the waveform sweep. Eq. (3) was inverted for each packet probability, then the square-law detector relation was solved for the two single-pulse SNR values. Their ratio determined the admissible deterministic mismatch loss. This calculation does not establish a probabilistic loss guarantee for a randomly varying chirp-rate error. Such a guarantee would require integration over the error distribution or a specified exceedance-probability constraint.

Hardware covariance would have to be estimated from synchronized, mean-removed source records in the coordinates used by the sensitivity model. Record length, bandwidth, temperature, and operating state affect that estimate. Common reference, clock, thermal, and supply paths can create off-diagonal terms. No such records were available in the present numerical study; Section 3.4 therefore uses an explicitly prescribed covariance matrix.

A production allocation would also require joint nonlinear verification with actual waveform, detector, timing, calibration, and environmental data. Biases would be applied with adverse signs, while random errors would follow the complete covariance model. Mean constraints and realization-level probability constraints must be tested separately. The present examples do not constitute that acceptance test. Sections 2.5–2.6 and the Appendix specify the numerical implementation and verification procedures for the normalized models.

3. RESULTS AND DISCUSSION

3.1 Detection-driven linear-frequency-modulated budget

For a 3-out-of-4 rule, Eq. (3) reduces to $H(p) = 4p^3 - 3p^4$. Solving $H(p_F) = 10^{-6}$ gave $p_F = 0.00630957367$ for each pulse. Solving $H(p_{D,0}) = 0.90$ and $H(p_{D,\min}) = 0.85$ gave 0.8574406833 and 0.8206156355. The normalized square-law threshold was $\eta = -2 \ln p_F = 10.13137434$. The SNR values were obtained by solving $Pr\{\chi'^2_2(2v) > \eta\} = p_D$, equivalently the Marcum-Q relation in Section 2.2. Bracketed scalar root finding over $0 \le v \le 50$ gave $v_0 = 8.45492488$ and $v_{\min} = 7.83331955$. Their SNR loss was $10 \log_{10}(v_0/v_{\min}) = 0.331639$ dB, with $a_{\min} = \sqrt{(v_{\min}/v_0)} = 0.962538$.

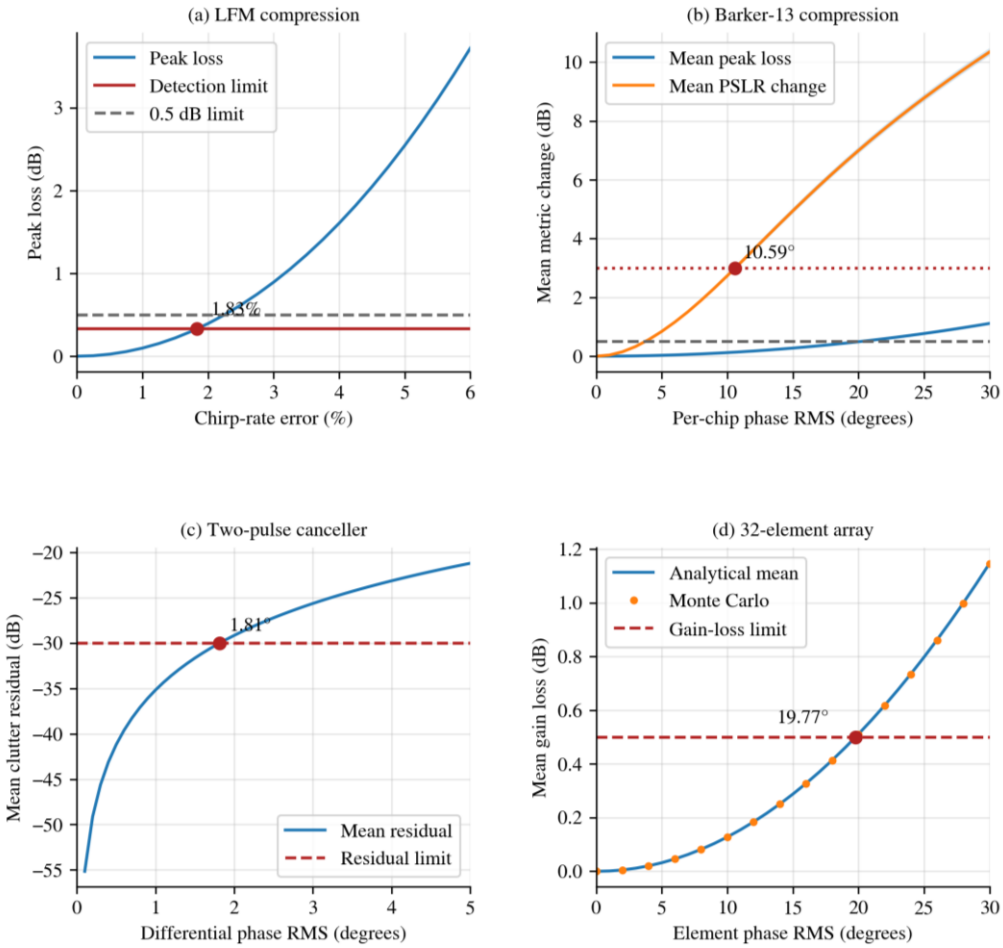


Figure 2. Normalized response curves
Note: Shading in Figure 2(b) shows pointwise 95% intervals for the mean.

Interpolation of the LFM loss curve at that level gave a prescribed chirp-rate-error boundary of 1.83% and a half-power width increase of 0.98%. A standalone 0.5 dB peak-loss limit gave 2.25% and a 1.81% width increase as shown in Figure 2(a). The detection condition therefore reduced the chirp-rate boundary by approximately 18.6% in this model. These are deterministic mismatch boundaries; they are not Gaussian error standard deviations.

3.2 Barker-13 compression

For Barker-13, the mean peak loss reached 0.5 dB at σ_b = 20.14°, whereas the mean PSLR degradation reached 3 dB at σ_b = 10.59°. The sidelobe metric therefore governed this case. At the bracketing levels of 10° and 11°, the standard errors of mean PSLR degradation were 0.0351 and 0.0388 dB. The corresponding pointwise approximate 95% interval half-widths were 0.0689 and 0.0761 dB. The peak-loss standard errors at 20° and 21° were 0.00572 and 0.00631 dB as shown in Figure 2(b). These results support a mean-response boundary, not a bound satisfied by every realization. No confidence interval for the interpolated phase boundary itself was estimated.

To map σ_b to hardware sources, let chip j have phase error $\theta_j = \sum r\ h_r u_{rj}$, where h_r converts source error u_{rj} into radians. Then $\sigma_b^2 = h\Sigma u\ h^T$ for each chip. The illustrative equal allocation assumes $h_r = 1$, four equal source variances, and independence both between sources and between chips. A phase term common to all chips rotates the compressed response but does not create the simulated sidelobe degradation. Consequently, the per-source value cannot be assigned to an oscillator without establishing its chip-to-chip covariance and transfer coefficients.

3.3 Moving-target-indication and active-array limits

The mean residual-power limit of 10^{-3} in Eq. (4) gave $\sigma_{\Delta\varphi} = \sqrt{[-2\ \ln(1 - 10^{-3}/2)]} = 0.0316267$ rad = 1.81° as shown in Figure 2(c). If consecutive pulse errors are independent with equal variance, the corresponding per-pulse RMS phase error is 1.28°. For correlated pulses, the relation in Section 2.3 must be used instead. The limit refers to the aggregate phase difference at the canceller input, not directly to an oscillator phase-noise specification.

For the array, solving Eq. (5) with $g = 10^{-0.05}$ gave an element RMS phase error σ_a = 19.77° as shown in Figure 2(d). Monte Carlo interpolation gave 19.79°, and the maximum analytical-to-simulation difference over the sweep was below 0.003 dB. These results concern mean coherent power gain only. Their numerical comparison with the MTI boundary does not imply interchangeable phase specifications: the MTI variable is a temporal phase difference, whereas the array variable is an independent element phase error. No beam-pointing or sidelobe criterion was tested.

3.4 Illustrative allocation in normalized error coordinates

For an additive zero-mean error coordinate $e = u_1 + u_2 + u_3 + u_4$, the illustrative sensitivity row is h = [1, 1, 1, 1]. Independent equal sources have covariance $\Sigma_u = (E^2/4)I_4$, where E denotes the aggregate RMS allowance, and I_4 is the identity matrix. Thus $\mathrm{Var}(e) = h\Sigma u\ h^T = E^2$, and each source has standard deviation $E/2$. Table 2 applies this arithmetic to the three phase-error coordinates. It gives 5.30° per source per chip for Barker-13, 0.91° per source for the MTI phase difference, and 9.89° per source per element for the array. Each value inherits the distribution and independence assumptions of its aggregate model.

Table 2. Aggregate boundaries and illustrative four-source shares

Error Coordinate	Aggregate Boundary	Illustrative Source Share
Linear-frequency-modulated (LFM) chirp rate	1.83% prescribed mismatch	0.92% formal root-sum-square (RSS) only; ≤0.4575% worst-case bias
Barker-13 chip phase	10.59° root-mean-square (RMS)	5.30° RMS per chip
Moving-target indication (MTI) phase difference	1.81° RMS	0.91° RMS differential phase
Array element phase	19.77° RMS	9.89° RMS per element

The LFM row requires a different interpretation. Its 1.83% limit is a prescribed deterministic mismatch, so 0.92% is only a formal RSS share in a hypothetical random-error model. It does not ensure the stated packet detection probability. For four equal deterministic contributions with adverse signs, a sufficient worst-case allocation based on the reported 1.83% boundary is at most 1.83%/4 = 0.4575% per source. A random chirp-rate allocation would need its own distribution-aware detection calculation.

For a separate correlation illustration, suppose only sources 1 and 2 correlate 0.30, while all four source variances remain $E^2/4$. The covariance is $\Sigma_u = (E^2/4)C$, where the rows of C are [1, 0.30, 0, 0], [0.30, 1, 0, 0], [0, 0, 1, 0], and [0, 0, 0, 1]. This matrix is positive definite, with eigenvalues 1.30, 0.70, 1, and 1. The aggregate variance is $h\Sigma u\ h^T = (E^2/4)(4 + 2 \times 0.30) = 1.15E^2$. The RMS factor is $\sqrt{1.15} = 1.0724$. Scaling all source standard deviations by $1/\sqrt{1.15} = 0.9325$ restores E. For the three stochastic phase cases, the illustrative shares become 4.94°, 0.85°, and 9.22°. The factor 1.15 follows only from this covariance and sensitivity row; it is not a general correction for correlated hardware.

3.5 Applicability and limitations

The numerical cases establish which of the imposed metrics becomes active in each normalized model. The packet detection condition restricted LFM chirp-rate mismatch more than the 0.5 dB peak-loss rule. Mean PSLR degradation restricted Barker-13 chip phase error more than mean peak loss. MTI depended on differential temporal phase, while the array calculation concerned mean gain under independent element errors. The equal-share and correlation examples establish the associated covariance arithmetic, not a measured system-level allocation.

Other waveforms can be investigated by defining their nominal signals, error coordinates, processing operators, and required metrics. Prior waveform and calibration studies [4-6, 11-12] provide possible contexts for such work. Their applicability would need to be checked for the chosen architecture. MIMO, frequency-diverse arrays, and integrated sensing and communication were not simulated here, so no compatibility or performance claim is made for those systems.

Practical use requires separate treatment of calibration bias,

random phase error, temporal correlation, and spatial correlation. A mean-gain limit does not constrain pointing or sidelobes. A confidence interval for an estimated mean does not provide a realization-level guarantee. Those additional criteria must be specified and verified before the illustrative source shares can be used as component requirements.

The evaluation was limited to the specified normalized LFM and Barker-13 signals, a two-pulse canceller, and an ideal broadside array. Measured component sensitivities, correlated chip-phase processes, non-Gaussian phase slips, amplifier memory, amplitude-to-phase conversion, oscillator spurs, quantization, and temperature dependence were not evaluated. A production study must retain the actual pulse duration, pulse-repetition interval, detector, array taper, calibration state, and hardware transfer functions. If the loss response is strongly nonlinear or an exceedance probability is prescribed, nonlinear uncertainty propagation is required instead of first-order loss linearization.

4. CONCLUSIONS

A mathematical framework was formulated to connect radar performance limits with signal-error coordinates and, where a stochastic source model is specified, source covariance. Its normalized examples showed that the governing constraint depends on the protected processing function. Detection loss, Barker-13 sidelobe degradation, MTI differential phase, and mean array gain therefore require distinct error definitions.

The equal-share calculations illustrate variance allocation under explicit unit-sensitivity and independence assumptions. The specified correlated-source example demonstrates how off-diagonal terms alter those shares. These results do not validate a complete radar or provide universal oscillator, clock, or array-channel specifications. Practical allocation requires measured source sensitivities and covariance, followed by verification of all applicable mean and probabilistic constraints in the nonlinear processing chain.

REFERENCES

[1] Marcum, J.I. (1960). A statistical theory of target detection by pulsed radar. IRE Transactions on Information Theory, 6(2): 59-267. https://doi.org/10.1109/TIT.1960.1057560

[2] Siddiq, K., Hobden, M.K., Pennock, S.R., Watson, R.J. (2019). Phase noise in FMCW radar systems. IEEE Transactions on Aerospace and Electronic Systems, 55(1): 70-81. https://doi.org/10.1109/TAES.2018.2847999

[3] Tschapek, P., Körner, G., Carlowitz, C., Vossiek, M. (2022). Detailed analysis and modeling of phase noise and systematic phase distortions in FMCW radar systems. IEEE Journal of Microwaves, 2(4): 648-659. https://doi.org/10.1109/JMW.2022.3195574

[4] Bharadwaj, N., Chandrasekar, V. (2012). Wideband waveform design principles for solid-state weather radars. Journal of Atmospheric and Oceanic Technology, 29(1): 14-31. https://doi.org/10.1175/JTECH-D-11-00030.1

[5] Torres, S.M., Curtis, C.D., Schvartzman, D. (2017). Requirement-driven design of pulse compression waveforms for weather radars. Journal of Atmospheric and Oceanic Technology, 34(6): 1351-1369. https://doi.org/10.1175/JTECH-D-16-0231.1

[6] Azouz, A., Abosekeen, A., Nassar, S., Hanafy, M. (2021). Design and implementation of an enhanced matched filter for sidelobe reduction of pulsed linear frequency modulation radar. Sensors, 21(11): 3835. https://doi.org/10.3390/s21113835

[7] Thurn, K., Ebelt, R., Vossiek, M. (2013). Noise in homodyne FMCW radar systems and its effects on ranging precision. In 2013 IEEE MTT-S International Microwave Symposium Digest (MTT), Seattle, WA, USA, pp. 1-3. https://doi.org/10.1109/MWSYM.2013.6697654

[8] Siddiq, K., Watson, R.J., Pennock, S.R., Avery, P., Poulton, R., Martins, S. (2016). Analysis of sampling clock phase noise in homodyne FMCW radar systems. In 2016 IEEE Radar Conference (RadarConf), Philadelphia, PA, USA, pp. 1-4. https://doi.org/10.1109/RADAR.2016.7485302

[9] Levy, C., Pinchas, M., Pinhasi, Y. (2021). Coherent integration loss due to nonstationary phase noise in high-resolution millimeter-wave radars. Remote Sensing, 13(9): 1755. https://doi.org/10.3390/rs13091755

[10] Birkenhauer, C., Tschapek, P., Vossiek, M. (2024). Over-the-air phase noise spectral density measurement for FMCW radar sensors. IEEE Journal of Microwaves, 4(4): 733-741. https://doi.org/10.1109/JMW.2024.3471803

[11] Geiß, J., Sippel, E., Braunwarth, M., Vossiek, M. (2023). The impact of antenna array calibration errors on MIMO and multi-channel synthetic aperture radar imaging. IEEE Journal of Microwaves, 3(2): 635-654. https://doi.org/10.1109/JMW.2023.3254135

[12] González-Coma, J.P., Nocelo López, R., Núñez-Ortuño, J.M., Troncoso-Pastoriza, F. (2025). Beacon-based phased array antenna calibration for passive radar. Remote Sensing, 17(3): 490. https://doi.org/10.3390/rs17030490

[13] Mohammed, J.R. (2022). Elements selection for auxiliary array in the adaptive sidelobe canceller radar system. Periodica Polytechnica Electrical Engineering and Computer Science, 66(4): 406-414. https://doi.org/10.3311/PPee.20452

[14] Schmid, C.M., Schuster, S.S., Feger, R., Stelzer, A. (2013). On the effects of calibration errors and mutual coupling on the beam pattern of an antenna array. IEEE Transactions on Antennas and Propagation, 61(8): 4063-4072. https://doi.org/10.1109/TAP.2013.2259455

NOMENCLATURE

a	normalized compressed-peak amplitude, dimensionless
B	waveform bandwidth, Hz
C	prescribed four-source correlation matrix, dimensionless
C_j	j-th radar-level characteristic
E	aggregate RMS allowance in an error coordinate
F_j	performance-to-metric mapping
G	hardware-error-to-metric mapping
g	normalized mean coherent array gain, dimensionless
h	source-to-error sensitivity row

$H(p)$	3-out-of-4 probability mapping, dimensionless
I_4	four-dimensional identity matrix
K	chirp rate, Hz s^{-1}
k	required number of detections
m	number of pulse decisions
M	nominal mainlobe interval
N	number of array elements
N_s	number of complex waveform samples
p_D, p_F	single-pulse detection and false-alarm probabilities
P_D, P_F	packet detection and false-alarm probabilities
q	vector of observable signal metrics
R	number of hardware-error sources
r_{MTI}	normalized residual clutter power, dimensionless
s_d	sample standard deviation of a simulated metric
S_{ir}	sensitivity of metric i to source r
$S_\varphi(f)$	one-sided phase PSD, rad^2 Hz^{-1}
s_0, s	nominal and perturbed complex waveforms
T	pulse duration, s
T_r	pulse-repetition interval, s
$t_{0.975,1199}$	Student t quantile for a pointwise 95% interval
u_{rj}	error from source r on chip j
x	vector of hardware errors
z_i	i-th selected signal metric
β_{ir}	fraction of allowable metric variance assigned to source r
δ	normalized peak sidelobe ratio, dimensionless
ΔC_j	admissible deterioration of C_j
$\Delta\tau$	relative half-power width increase, dimensionless
$\Delta\varphi_n$	$\varphi_n - \varphi_{n-1}$, rad
ε_K	relative chirp-rate error, dimensionless
η	normalized square-law threshold, dimensionless
θ_j	phase error of chip j, rad
ν	signal-to-noise ratio, dimensionless
ρ_1	lag-one phase correlation, dimensionless
σ_a	RMS element phase error, rad
σ_b	RMS per-chip phase error, rad
σ_p	RMS phase error of an individual pulse, rad
Σ_u	covariance of the illustrative source errors
Σ_x	hardware-error covariance matrix
$\sigma_{\Delta\varphi}$	RMS differential inter-pulse phase error, rad
τ	delay, s
φ_n	residual phase of pulse n, rad
φ_ℓ	phase error of element ℓ, rad

Abbreviations

FMCW	frequency-modulated continuous wave
LFM	linear frequency modulation
MIMO	multiple-input multiple-output
MTI	moving-target indication
PCG64	permutedcongruentialgeneratorwith64-bitoutput
PSLR	peak sidelobe ratio
PSD	power spectral density
RMS	root-mean-square
RSS	root-sum-square
SNR	signal-to-noise ratio

APPENDIX

A. Numerical implementation

Calculations and figure generation used Python with NumPy 2.3.5, SciPy 1.17.0, and Matplotlib 3.10.8. Analytical responses and Monte Carlo simulations were evaluated for the normalized signal models.

Independent PCG64 generators, each initialized with seed 2026, were used for Barker-13 and the array. Each generator produced one complete standard-normal matrix, reused at all error levels. The array results therefore did not depend on the Barker draw count. Linear full-length convolution was used without circular wrapping.

The decibel conventions were as follows: compressed-peak loss is $-20\log_{10}$ of normalized amplitude; array loss is $-10\log_{10}$ of the mean normalized power; and MTI residual is $10\log_{10}$ of mean normalized residual power. Barker PSLR degradation is calculated in decibels for each realization before averaging. Positive compression and array losses indicate deterioration in Figure 2.

Numerical verification checked packet-probability roots, nominal Barker PSLR, the analytical MTI and array boundaries, and agreement between Monte Carlo and analytical array means. These checks concern the normalized models within the scope defined in Section 3.5.